



# Remote Sensing of Tropospheric Turbulence Using GPS Radio Occultation

Esayas Shume<sup>1,2</sup> and Chi Ao<sup>1</sup>

<sup>1</sup>Jet Propulsion Laboratory, California Institute of Technology, Pasadena, CA, USA

<sup>2</sup>Department of Astronomy, California Institute of Technology, Pasadena, CA, USA

*Correspondence to:* Esayas Shume (Esayas.B.Shume@jpl.nasa.gov)

**Abstract.** Radio occultation (RO) measurements are sensitive to the small-scale irregularities in the atmosphere. In this study, we present a new technique to estimate tropospheric turbulence strength (namely, scintillation index) by analyzing RO amplitude fluctuations in impact parameter domain. GPS RO observations from the COSMIC (Constellation Observing System for Meteorology, Ionosphere, and Climate) satellites enabled us to calculate global maps of scintillation measures, revealing the seasonal, latitudinal, and longitudinal characteristics of the turbulent troposphere. Such information are both difficult and expensive to obtain especially over the oceans. To verify our approach, simulation experiments using the multiple phase screen (MPS) method were conducted. The results show that scintillation indices inferred from the MPS simulations are in good agreement with scintillation measures estimated from COSMIC observations.

## 1 Introduction

Atmospheric turbulence associated with fluctuation of temperature, humidity, and water vapor are prevalent in the tropospheric region. Irregularities in the turbulence cause the index of refraction of the tropospheric medium to fluctuate. Electromagnetic signals transmitted from Global Navigation Satellite System (GNSS) satellites (for example), carrying communication and navigation information, propagate through the turbulent troposphere. The spatial changes of the index of refraction introduce irregular fluctuations in the intensity and phase of the traversing electromagnetic signals by causing scintillation (Wheelon, 2004). Signal scintillation can affect the performance of satellite communication and navigation systems such as Global Positioning System (GPS). On the other hand, scintillation characteristics inferred from global GPS signal observations (employed here) are valuable resources to study atmospheric turbulence properties.

In this paper, we have employed data analysis and model simulation to investigate and quantify the effects of tropospheric turbulence on L-band signals propagating from a GPS satellite to a low earth orbit (LEO) satellite such as COSMIC (Constellation Observing System for Meteorology, Ionosphere, and Climate) (Anthes *et al.*, 2008). We estimated global distribution of the turbulence strength using a scintillation parameter (scintillation index) from COSMIC Radio Occultation (RO) measurements. To understand and quantify the observed scintillation, we have simulated the effect of tropospheric turbulence on L-band signals propagating through multiple phase screens (MPS). In the MPS model runs, the phase screens are assumed



to be various realizations of random perturbations of index of refraction profiles through which electromagnetic waves are propagating (Knupp, 1983).

## 2 Global Scintillation Maps Inferred from COSMIC RO Measurements

This section presents investigation of the effect of tropospheric turbulence on L-band propagation utilizing RO observations 5 from a GPS to a COSMIC satellites radio links. We estimated the impact of turbulence strength on L-band signals in terms of scintillation index. The COSMIC satellites provide a significant number of RO profiles (up to about 2000 profiles per day) observed by the six micro-satellites covering the entire globe. Utilizing the RO profiles, we were able to estimate the global distribution of the effect of scintillation on GPS signals. The technique provides valuable scintillation data especially over the 10 oceans where ground-based measurements are both difficult and expensive to perform. RO data were first used to determine the intensity and location of turbulent regions (Cornman *et al.*, 2012). Our study differs in that we aim to study the global 15 climatology of tropospheric turbulence. In addition, we suggest that a different observable than raw amplitude and phase measurements is more effective in estimating scintillation index.

### 2.1 COSMIC signal amplitude measurements

The basic observations of RO soundings on COSMIC are time series of amplitude (the 1-second voltage signal-to-noise ratio) 15 and phase of L-band signals transmitted by a GPS satellite (e.g., Hajj *et al* (2002)). As the radio signal propagates through the troposphere, the amplitude of the signal (raw amplitude) suffers from the effects of defocusing, multipath propagation, and diffraction effects. Therefore, the raw amplitude fluctuation does not truly represent the effect of turbulence. To suppress 20 amplitude fluctuations due to these effects, the canonical transform (CT) has been applied on the received complex signal to transform it from the time domain to the impact parameter domain (Gorbunov, 2002). In RO retrieval processing, the CT phase is considered the important quantity since it is used to retrieve the bending angle profile and subsequently the refractivity 25 profile, which are the primary retrieval variables. In our study, however, the focus is on the CT amplitude. We assume that CT amplitude fluctuations are dominated by small-scale irregularities caused by turbulent processes.

We note that CT operates under the assumption of a spherically symmetric atmosphere where each ray is uniquely identified by its impact parameter. Thus the presence of mesoscale or large-scale horizontal inhomogeneity can result in fluctuations in 25 the CT amplitudes; however, these tend to occur at a larger spatial scales than the turbulent effects being considered so that their contribution to the scintillation estimates is expected to be small.

### 2.2 Scintillation Effects on COSMIC RO Signals

The scintillation index  $\sigma_I$  can be viewed as a measure of the effect of tropospheric turbulence on L-band propagation having signal intensity  $I$ .  $\sigma_I$  can be described as a normalized standard deviation of intensity  $I$  fluctuation:

$$30 \sigma_I = \left( \frac{\langle I^2 \rangle - \langle I \rangle^2}{\langle I \rangle^2} \right)^{\frac{1}{2}} \quad (1)$$



where  $\langle \dots \rangle$  stands for expected value and  $I$  is the CT intensity, which is the square of the CT amplitude. The expected value is computed using data in 120 m intervals.

### 2.2.1 Scintillation Index Estimates

5 Figures 1 and 2 shows global maps of  $\sigma_I$  estimated by applying equation 1 on the CT intensity computed from the COSMIC RO measurements.

In the global map of scintillation estimates presented in Figures 1, the scintillation index is an altitudinal average of  $\sigma_I$  between altitudes 1 to 4 km. Figure 2 shows an average of  $\sigma_I$  between 4 and 8 km. In this study, we restrict our results to above 10 1 km due to possible data quality issues affecting the near-surface retrievals (Ao *et al.*, 2012). The global scintillation maps presented in Figures 1 and 2 are for the months of January, April, July, and October of the year 2008. To construct these global scintillation maps, about 60,000 RO profiles were employed. The results can be easily extended to other periods.

The scintillation maps (Figures 1 & 2) contain a wealth of valuable information. Figures 1 and 2 show similar geographic and seasonal patterns; however, the values of  $\sigma_I$  are significantly higher at the lower altitudes shown in Fig. 1. This is due to the sensitivity of the radio signals to the water vapor irregularities in the lower troposphere and as a result signal scintillations 15 are more frequently observed between the top of the boundary layer and 4 km (cf. Fig. 3 of Sokolovskiy (2001) and Fig. 2 of Beyerle *et al* (2008), for example). From the scintillation maps, the followings can be noted:

1. The effects of the tropospheric turbulence on L-band propagation have a very strong seasonal dependence. Summer hemispheres show significant turbulent activities (measured by  $\sigma_I$ ) compared to winter hemispheres (Figures 1A & 1C, and Figures 2A & 2C). The magnitude of the global L-band scintillation is relatively large in the summer hemisphere 20 compared to the winter hemisphere. Increased turbulence activities due to surface heating could be a reason for higher scintillation in the summer hemisphere. This property is also consistent with the global distribution of precipitation content, which has relatively significant magnitude during summer (Adler *et al*, 2003; Xie *et al*, 1997).
2. Figures 1 and 2 show that irrespective of seasons, the tropical regions are characterized by a relatively large  $\sigma_I$  possibly due to the concentration of significant amount of water vapor in the lower tropical troposphere.
- 25 3. Using  $\sigma_I$  as a proxy for turbulence strength, we infer that the northern hemisphere summer (July 2008, Figures 1C and 2C) shows relatively large turbulent activities compared to the southern hemisphere summer (Jan 2008, Figures 1A & 2A). During the respective summer months, the Antarctic region is characterized by less turbulence strength compared to the Arctic region. This is most pronounced in the temperate and polar regions. The effect of the Arctic sea and the high altitude of the Antarctic, make the Arctic polar region relatively warmer than the Antarctic region. The warm air in 30 the Arctic holds more moisture than the cold air in the Antarctic. Temperature fluctuations could also cause the observed differences.



4. The scintillation estimates for the equinox seasons [Figures 1B & 2B (April 2008) and Figures 1D & 2D (Oct 2008)] are symmetrical about the equator. Scintillation estimates in the tropics are fairly symmetrical for all seasons.
5. The troposphere over the Sahara region is characterized by low scintillation effects on L-band propagation compared to the neighboring regions to its east and west. The water vapor content is consistently low and the air is dry over the Sahara (Schrijver *et al.*, 2009). A close comparison of the maps (Figures 1A-D & 2A-D) shows that the strength of scintillation is relatively enhanced during July (summer) over the Sahara due to relatively hotter air.
10. Figures 1A-D & 2A-D clearly demonstrate an ocean-continent contrast of the scintillation estimates in the Southern East Pacific, South America, and South Atlantic regions. Over these regions, the average  $\sigma_I$  is low over the ocean compared to the continent. These  $\sigma_I$  oscillations are highly correlated with (i) the convective available potential energy (CAPE) whose values are maximum over the continent (Riemann-Campe *et al.*, 2009), and (ii) atmospheric relative humidity from satellite data (Du *et al.*, 2012).
15. The turbulence strength difference between summer and winter seasons over the Antarctica is small compared to the turbulence strength difference between summer and winter seasons over the Arctic. Similar results based on radiosonde, satellite, and atmospheric reanalyses observation were reported (Serreze *et al.*, 2012; Bromwich *et al.*, 2007). Compared to other regions, the Arctic and Antarctic have the least observations available. The RO inferred map presented in Figures 1 and 2, therefore, helps to build and enrich the polar region database.
8. For all seasons,  $\sigma_I$  changes significantly with season in the North-East Pacific compared to South-East Pacific.

### 2.2.2 The Index of Refraction Structure Parameter

The index of refraction structure parameter  $C_n^2$  is valuable for investigating propagation of electromagnetic waves in the atmosphere. Amplitude and phase of the waves propagating through the atmosphere get degraded as  $C_n^2$  is intensified (Andreas *et al.*, 1989). Unfortunately, measuring  $C_n^2$  is expensive and difficult to perform, especially over the oceans. Due to that  $C_n^2$  profiles are available from only a few locations over the globe ((Andreas *et al.*, 1989; Wheelon, 2004) and the references). RO offers the possibility of filling these gaps. Here, we present  $C_n^2$  profiles inverted from CT amplitude scintillation incurred on COSMIC RO observations and the Rytov variance (equation 2).

25. Assuming that the wavelength of propagation is small compared to the scale of index of refraction fluctuations,  $\sigma_I$  can be expressed in terms of turbulence properties ( $C_n^2$ ) of the medium by the Rytov variance. The Rytov variance assumes wave propagation in weak fluctuation regimes ( $\sigma_I^2 < 1$ ) caused by turbulence processes having characteristics of Kolmogorov spectra. Since the amplitude of fluctuations of the RO signals considered are characterized by  $\sigma_I^2 < 1$ , the Rytov variance is valid for the present analysis. Note that the Rytov variance was used to describe characteristics of weak scintillation of radio and 30 microwave propagation in the atmosphere (Clifford and Strohbehn, 1970; Woo and Ishimaru, 1973; Ishimaru, 1978; Martini *et al.*, 2006; Blaustein and Christodoulou, 2007). For plane waves,  $\sigma_I^2$  is proportional to  $C_n^2$  (Andrews *et al.*, 1999):

$$\sigma_I^2 = 1.23 C_n^2 \kappa_{\circ}^{\frac{7}{6}} L^{\frac{11}{6}}, \quad C_n^2 = 0.813 \sigma_I^2 \kappa_{\circ}^{-\frac{7}{6}} L^{-\frac{11}{6}}, \quad \kappa_{\circ} = \frac{2\pi}{\lambda} \quad (2)$$



$\kappa_o$  is wavenumber of the electromagnetic wave,  $\lambda$  is wavelength, and  $L$  is the propagation path length between a transmitter and a receiver through the turbulent medium.

The  $C_n^2$  profile can be calculated from  $\sigma_I^2$  profile for each occultation by making use of equation 2 with  $\lambda = 0.2\text{ m}$  and  $\kappa_o = 31.4\text{ m}^{-1}$ . Figure 3A, 3B, and 3C show the distribution of  $\sigma_I^2$  averaged over 1 to 8 km in the tropics, mid-latitude, and 5 high-latitude troposphere, respectively. The histograms reveal that about 95% of the  $\sigma_I^2$  values are less than 1 in Figure 3A. The distribution of  $\sigma_I^2$  shows values less than 1 more 95% of the cases.. Since measured  $\sigma_I^2 < 1$  in Figures 1 and 2 predominantly, the application of the Rytov variance is justified for estimating  $C_n^2$  profile. To compute  $C_n^2$  profiles from  $\sigma_I^2$  profiles, we still have to know the value of an effective signal propagation length  $L$  in the lower troposphere corresponding to RO geometry. For that purpose,  $L$  has been estimated using a multi phase screen (MPS) model simulation technique described in Section 3. We 10 use the MPS model to calculate the scintillation index  $\sigma_I^{2_{model}}$  by varying the value of  $C_n^2$  (the MPS model runs use index of refraction as input derived from Kolmogorov spectra, equations 3 and 4). We used the following procedures in the MPS model to estimate  $L$ : The relationship between the scintillation index  $\sigma_I^{2_{model}}$  and  $C_n^2$  is linear (equation 2). Using linear regression, we determine the slope in the  $\sigma_I^{2_{model}}$  and  $C_n^2$  relationship. The propagation path length  $L$  is estimated from the slope, and have an average value of  $L = 650\text{ km}$  in the lower troposphere. We recognize that  $L$  is not exactly a constant and would vary with 15 altitudes and differ from sounding to sounding; however, we expect using a single average  $L$  to estimate  $C_n^2$  for all occultations to be a good approximation to first order.

Figure 4 depicts representative  $C_n^2$  profiles calculated utilizing COSMIC RO signal amplitudes received over the Central Pacific, New Mexico, South East Pacific, and Arctic (North of Alaska) in January and July 2008. The  $C_n^2$  profiles are averaged over  $5^\circ$  latitude and  $5^\circ$  longitude. The  $C_n^2$  profiles, estimated from COSMIC RO, shown in Figure 4 decrease with altitude in the 20 lower troposphere in agreement with measured  $C_n^2$  profiles ((*Andreas et al.*, 1989; *Wheelon*, 2004), for example). Specifically, in Figures 4A, 4B and 4D (Central Pacific, New Mexico, and Arctic (North of Alaska)), the  $C_n^2$  profiles show clear seasonal behavior (summer-winter contrast).  $C_n^2$  is larger in the July compared to January (New Mexico and Arctic (North of Alaska), Figure 4B & 4D). It is larger in January compared to July (South East Pacific, Figure 4C). On the other hand,  $C_n^2$  is only a little larger in July compared to January (Central Pacific, Figure 4A). The mean  $C_n^2$  value ( $0.25 \times 10^{-14}\text{ m}^{-2/3}$ ), reported in 25 (*Wheelon* (2004) and the references therein), agrees with an approximate mean summer values of  $C_n^2$  displayed in Figures 4B and 4D.

### 3 Wave Propagation Simulations

#### 3.1 Multiple Phase Screen (MPS) Model

The merit of the phase screen technique to find solution of electromagnetic wave propagation through turbulent medium has 30 been described in the literature (e.g., (*Knepp*, 1983; *Knepp and Lickisch*, 2009)). In the context of this paper, the MPS model is applied to simulate and quantify the effect of tropospheric turbulence (and the resulting index of refraction variations) on L-band propagation. The MPS technique employed uses the geometry of L-band propagation in a radio link from a GPS satellite (incident wave) to a low-Earth orbit satellite (receiver, observation screen) (*Sokolovskiy*, 2001).



The MPS technique involves finding the solution of the parabolic wave equation (Kneppe, 1983; Kneppe and Lickisch, 2009). The solution comprises application of numerical and Fourier transform techniques repeatedly for waves propagating through MPSs (Kneppe, 1983; Kneppe and Lickisch, 2009) idealized by parallel planes (phase changing screens). The medium of signal propagation is divided into a number of thin layers, each modeled as phase changing screens encompassed by a free space. 5 Accordingly, we seek solution of the parabolic equation by performing successive iteration of the propagation calculations from one screen to the next, and ultimately to the observation screen.

### 3.2 Model Results and Discussion

#### 3.2.1 Index of Refraction Profiles: Model Input

The main input for the MPS model run is an index of refraction profile of the lower troposphere. The phase screens are 10 constructed as random perturbations of an exponential background refractivity profile (first term in equation 3):

$$N(y) = N_0 \exp\left(-\frac{y}{H_s}\right) + \tilde{N}(y) \quad (3)$$

where the index of refraction profile  $n(y)$  is calculated from the refractivity profile using  $N(y) = 10^6[n(y) - 1]$ ,  $N(0) = N_0 = 320$ , and the scale height  $H_s = 7$  km. The resulting background refractivity is shown in Figure 5A. In the refractivity perturbation models ( $\tilde{N}(y)$ ), tropospheric turbulence is taken to be nonzero only up to 8 km.  $\tilde{N}(y)$  is an inverse Fourier 15 transform of the Kolmogorov spectra (equation 4) modulated by a Gaussian random number with zero mean and standard deviation one (Kneppe, 1983). In order to make the refractivity perturbations realistic, the refractivity profiles on the phase changing screens are specified by the characteristics of Kolmogorov spectra,

$$\hat{\Phi}(\kappa) = 0.033C_n^2\kappa^{-\frac{11}{3}}, \quad \kappa = \frac{2\pi}{y} \quad (4)$$

Figure 5B shows example refractivity profiles calculated using equation 4 (an input for the MPS model runs).

#### 20 3.2.2 Input Parameters for MPS model runs

The input parameters for MPS model runs were: Number of phase screens = 4000; vertical spacing = 1 m; spacing between phase screens = 1 km; a Gaussian random number initializes each phase screen differently; on each phase screen, each altitude is initialized differently.

#### 3.2.3 Scintillation Index Profiles: MPS model

25 The MPS model runs were performed for two cases where: (a)  $C_n^2 = 1.0 \times 10^{-13} m^{-2/3}$  and (b)  $C_n^2 = 5.0 \times 10^{-14} m^{-2/3}$ . For each case, 50 random realizations of the MPS runs were used to calculate CT amplitude profiles. The average CT intensity profiles (average of the 50 CT intensity profiles) were then used to calculate  $\sigma_I$  profiles every 50 m in the lower troposphere (shown in Figure 5C).

For comparison and validation purposes, Figure 5D plots  $\sigma_I$  profiles estimated from COSMIC RO data over Central Pacific, 30 New Mexico, Arctic (North of Alaska), and South East Pacific. The MPS inferred  $\sigma_I$  profiles are in a reasonable agreement



with the COSMIC RO inferred  $\sigma_I$ . Figures 5C and 5D show a very good agreement between the MPS model  $\sigma_I$  - COSMIC RO  $\sigma_I$  over the Central Pacific (January and July 2008) and New Mexico (July 2008). Figure 5E presents  $C_n^2$  estimates derived from  $\sigma_I^2$  profiles (MPS model, Figure 5C). The Rytov variance has been used to invert for the  $C_n^2$  profiles. Figure 5E reproduces the input  $C_n^2$  values fairly well. The  $C_n^2$  profiles shown in Figure 5E have similarities with the  $C_n^2$  profiles shown in Figure 4 5 validating  $C_n^2$  profiles derived from COSMIC RO data. In Figure 5E, the blue vertical line shows  $C_n^2 = 5.0 \times 10^{-14} \text{ m}^{-2/3}$  and the brown vertical line shows  $C_n^2 = 1.0 \times 10^{-14} \text{ m}^{-2/3}$ . The decrease of  $C_n^2$  starting  $\sim 6$  km is believed to be due to the finite vertical extent of the turbulence model in the MPS simulation.

#### 4 Conclusions

We have used (i) radio occultation observations on board the COSMIC satellites, and (ii) multiple phase screen model calculations to investigate and quantify the effect of tropospheric turbulence on L-band propagation. Instead of regular amplitude and phase data, we have used the CT amplitudes in estimating the scintillation indices from each occultation. This has the advantage of removing signal fluctuations due to atmospheric multipath and diffraction from sharp vertical layers.

Global maps of scintillation measures across different seasons were obtained from one year of COSMIC RO data. The resulting global scintillation maps reveal very strong seasonal dependence, with the northern hemisphere summer exhibiting 15 relatively large turbulent activities compared to the southern hemisphere summer. Irrespective of seasons, the tropical regions are generally characterized by a relatively large scintillation index. The maps also show clear ocean-continent contrast of the scintillation estimates in the Southern East Pacific, South America, and South Atlantic regions. The scintillation estimates appear to be positively correlated with water vapor, precipitation, and convection. We have also presented  $C_n^2$  profiles estimated from COSMIC RO data using the Rytov variance method for weak scintillation. This represents the first ever observational 20 estimates of global tropospheric turbulence strength. While certain simplifications have been used in this initial study, the results are encouraging, and future work can be done to refine the results and cross-validate with other observations.

We have also performed numerical simulations of radio propagation through a random phase changing screen (in which refractivity profiles were specified by the Kolmogorov spectra). Scintillation index profiles inferred from the MPS technique are in a reasonable agreement with scintillation index profiles inferred from COMSIC RO data and provide confidence to our 25 estimates of  $C_n^2$  profiles

*Author contributions.* E. B. Shume and C. O. Ao contributed in COSMIC RO data analysis, Multiple Phase Screen simulation, and writing this paper.

*Acknowledgements.* The research was carried out at the Jet Propulsion Laboratory, California Institute of Technology, under a contract with NASA.



## References

Adler, R. F., George J. Huffman, Alfred Chang, Ralph Ferraro, Ping-Ping Xie, John Janowiak, Bruno Rudolf, Udo Schneider, Scott Curtis, David Bolvin, Arnold Gruber, Joel Susskind, Philip Arkin, and Eric Nelkin, 2003, The Version-2 Global Precipitation Climatology Project (GPCP) Monthly Precipitation Analysis (1979–Present). *J. Hydrometeor.*, 4, 1147–1167.

5 Andreas, E. L. (1989), The refractive index structure parameter,  $C_n^2$ , for a year over the frozen Beaufort Sea, *Radio Sci.*, 24(5), 667–679, doi:10.1029/RS024i005p00667.

Andrews, L. C., R. L. Phillips, C. Y. Hopen, and M. A. Al-Haresh, Theory of optical scintillation, *J Opt. Soc. Am. A*, Vol. 16, No. 6, 1999.

Anthes, R. A. et al., 2008: The COSMIC/FORMOSAT-3 Mission: Early Results. *Bull. Amer. Meteor. Soc.*, 89, 313–333. doi: <http://dx.doi.org/10.1175/BAMS-89-3-313>.

10 Ao, C. O., D. E. Waliser, S. K. Chan, J.-L. Li, B. Tian, F. Xie, and A. J. Mannucci, 2012, Planetary boundary layer heights from GPS radio occultation refractivity and humidity profiles. *J. Geophys. Res.*, 117, D16117, doi:10.1029/2012JD017598.

Beyerle, G., M. E. Gorbunov, and C. O. Ao (2003), Simulation studies of GPS radio occultation measurements, *Radio Sci.*, 38(5), 1084, doi:10.1029/2002RS002800.

Blaunstein, N. and C. Christodoulou (2007), Radio Propagation and Adaptive Antennas for Wireless Communication Links Terrestrial, 15 Atmospheric and Ionospheric WILEY INTERSCIENCE A JOHN WILEY and SONS, INC. PUBLICATION.

Bromwich, D. H., R. L. Fogt, K. I. Hodges, and J. E. Walsh (2007), A tropospheric assessment of the ERA-40, NCEP, and JRA-25 global reanalyses in the polar regions, *J. Geophys. Res.*, 112, D10111, doi:10.1029/2006JD007859.

Clifford, S. F. and J. W. Strohbehn (1970), The theory of microwave line-of-sight propagation through a turbulent atmosphere, *IEEE Trans. Antenn. Prop.*, AP-18, 264 - 274.

20 Cornman, L. B., Goodrich, R. K., Axelrad, P., and Barlow, E.: Progress in turbulence detection via GNSS occultation data, *Atmos. Meas. Tech.*, 5, 789-808, doi:10.5194/amt-5-789-2012, 2012.

Du, J., F. Cooper, and S. Fueglister (2012), Statistical analysis of global variations of atmospheric relative humidity as observed by AIRS, *J. Geophys. Res.*, 117, D12315, doi:10.1029/2012JD017550.

Gifford, F. A. (1988), A Similarity Theory of the Tropospheric Turbulence Energy Spectrum, *J. Atmos. Sci.*, 45, 1370-1379. doi: 25 [http://dx.doi.org/10.1175/1520-0469\(1988\)0451370:ASTOTT2.0.CO;2](http://dx.doi.org/10.1175/1520-0469(1988)0451370:ASTOTT2.0.CO;2)

Gorbunov, M. E., Canonical transform method for processing radio occultation data in the lower troposphere, *Radio Sci.*, 37(5), 1076, doi:10.1029/2000RS002592, 2002.

Hajj, G. A., E.R. Kursinski, L.J. Romans, W.I. Bertiger, and S.S. Leroy (2002), A technical description of atmospheric sounding by GPS occultation, *Journal of Atmospheric and Solar-Terrestrial Physics*, 64, 451 - 469, DOI:10.1016/S1364-6826(01)00114-6

30 Ishimaru, A. (1978), Wave Propagation and Scattering in Random Media. Multiple Scattering, Turbulence, Rough Surfaces, and Remote Sensing ACADEMIC PRESS New York San Francisco London, Volume 2.

Knepp, D. L. 1983, Multiple phase-screen calculation of the temporal behavior of stochastic waves, *Proceedings of the IEEE*, 71, 6 , 722 - 737, doi: 10.1109/PROC.1983.12660.

Knepp, D. L., and L. J. Nickisch (2009), Multiple phase screen calculation of wide bandwidth propagation, *Radio Sci.*, 44, RS0A09, 35 doi:10.1029/2008RS004054.

Martini, E., A. Freni, and F. Cuccoli (2006), Impact of Tropospheric Scintillation in the Ku/K Bands on the Communications Between Two LEO Satellites in a Radio Occultation Geometry, *IEEE TRANSACTIONS ON GEOSCIENCE AND REMOTE SENSING*, VOL. 44, NO. 8.



Riemann-Campe K, Fraedrich K, and Lunkeit F. (2009), Global climatology of convective available potential energy (CAPE) and convective inhibition (CIN) in ERA-40 reanalysis, *Atmospheric Research* 93: 534-545, DOI: 10.1016/j.atmosres.2008.09.037.

Schrijver, H., Gloudemans, A. M. S., Frankenberg, C., and Aben, I. (2009), Water vapour total columns from SCIAMACHY spectra in the 2.36  $\mu\text{m}$  window, *Atmos. Meas. Tech.*, 2, 561-571, doi:10.5194/amt-2-561-2009.

5 Serreze, M. C., A. P. Barrett, and J. Stroeve (2012), Recent changes in tropospheric water vapor over the Arctic as assessed from radiosondes and atmospheric reanalyses, *J. Geophys. Res.*, 117, D10104, doi:10.1029/2011JD017421.

Sokolovskiy, S. V. (2001), Modeling and inverting radio occultation signals in the moist troposphere, *Radio Sci.*, 36(3), 441-458, doi:10.1029/1999RS002273.

10 Sokolovskiy, S. V., C. Rocken, D. H. Lenschow, Y.-H. Kuo, R. A. Anthes, W. S. Schreiner, and D. C. Hunt (2007), Observing the moist troposphere with radio occultation signals from COSMIC, *Geophys. Res. Lett.*, 34, L18802, doi:10.1029/2007GL030458.

Wheelon, A., *Electromagnetic Scintillation I. Geometric Optics*, Cambridge, UK: Cambridge University Press, 2004.

Woo, R., and A. Ishimaru (1973), Remote sensing of the turbulence characteristics of a planetary atmosphere by radio occultation of a space probe, *Radio Sci.*, 8(2), 103-108, doi:10.1029/RS008i002p00103.

Xie, P. and Phillip A. Arkin, 1997, Global Precipitation: A 17-Year Monthly Analysis Based on Gauge Observations, Satellite Estimates, and  
15 Numerical Model Outputs, *Bull. Amer. Meteor. Soc.*, 78, 2539-2558.

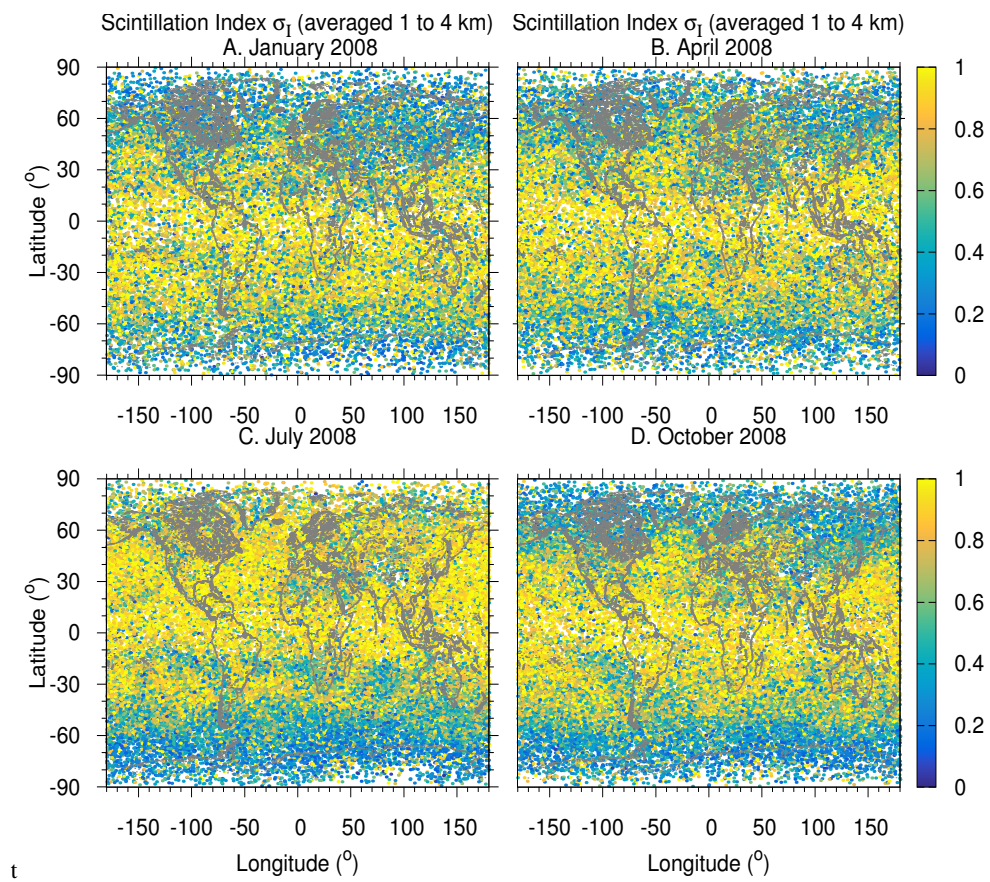


**Figure 1.** Global map of altitudinal average (1 to 4 km altitudes) scintillation index derived from the COSMIC RO data for January, April, July and October 2008.

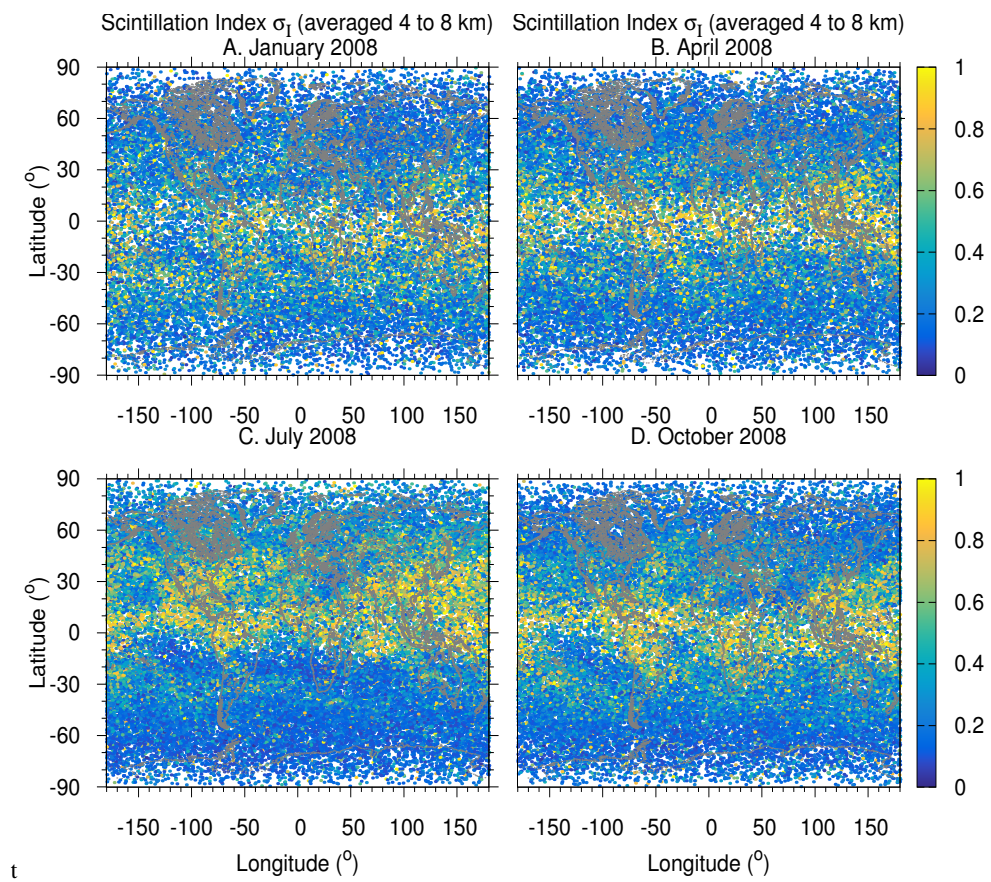


**Figure 2.** Global map of altitudinal average (4 to 8 km altitudes) scintillation index derived from the COSMIC RO data for January, April, July and October 2008.



t

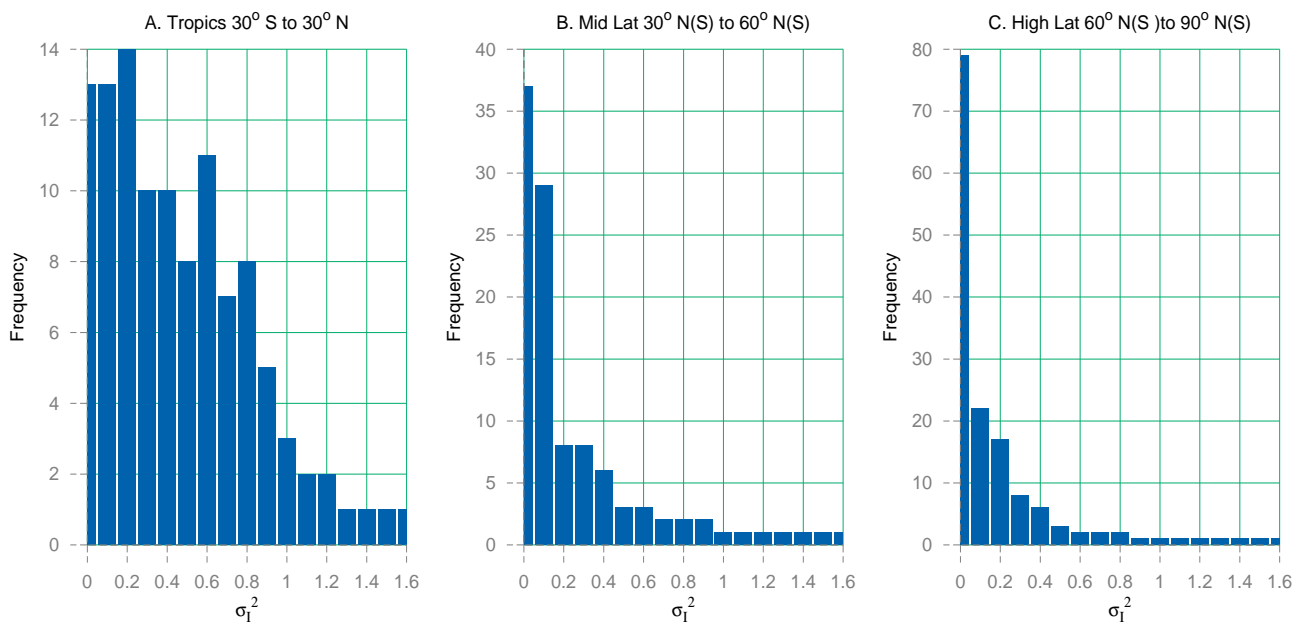


**Figure 3.** Histogram of  $\sigma_I^2$  COSMIC RO averaged 1 to 8 km: (A) Tropics, (B) Mid-Latitude, and (c) High-Latitude.



t

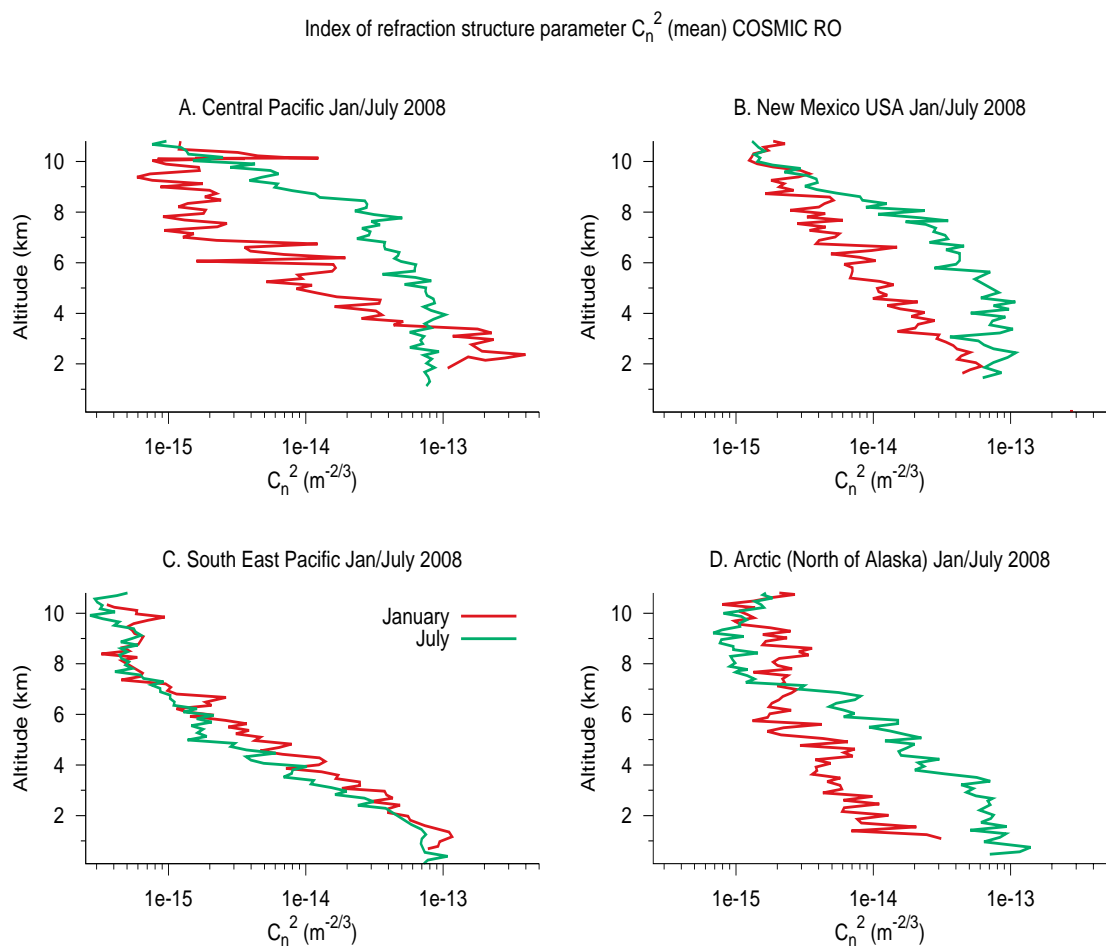


**Figure 4.** The index of refraction structure parameter  $C_n^2$  inferred from CT signal amplitude of COSMIC RO data.



t

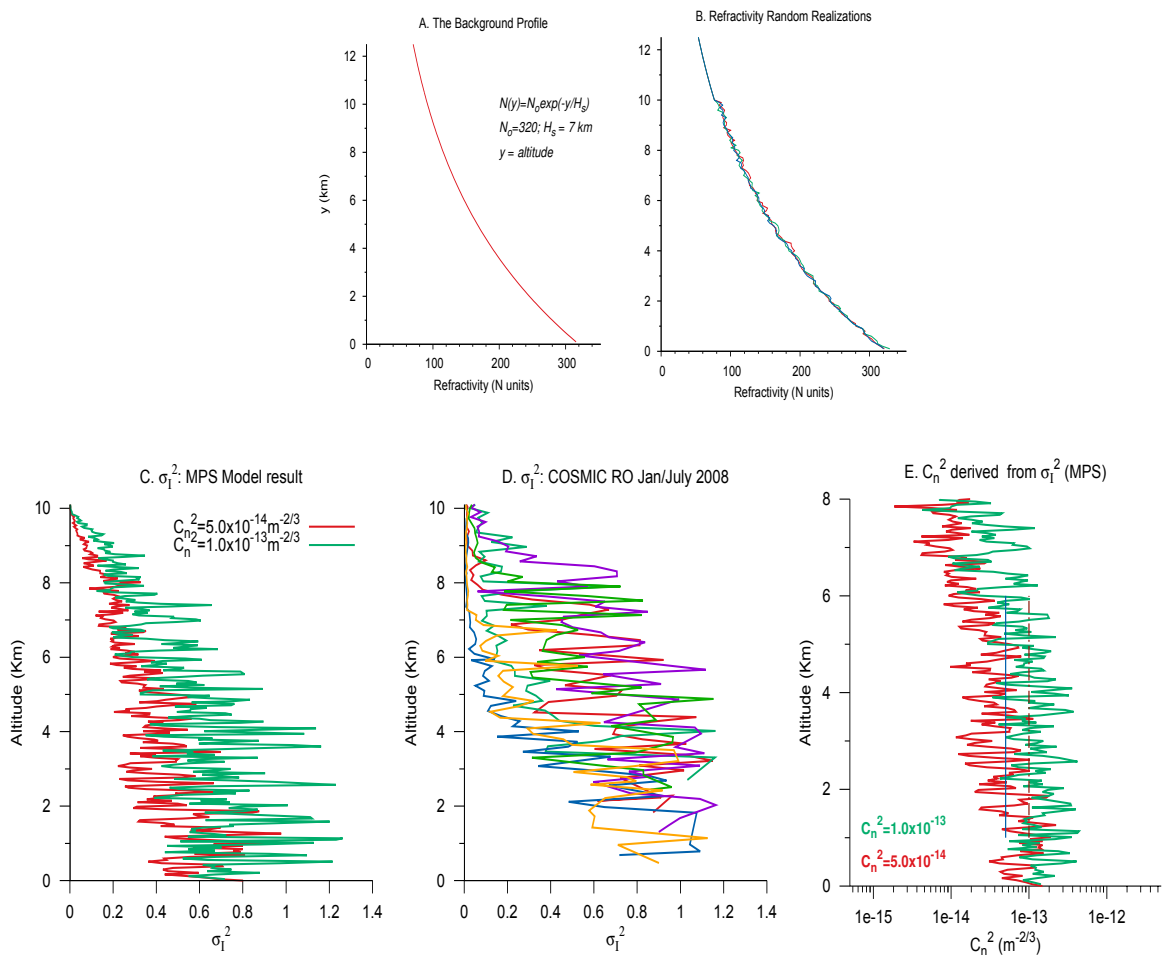


**Figure 5.** (A) and (B) Example refractivity profile employed as an input for the multi phase screen (MPS) simulation runs. (C) Scintillation index  $\sigma_I^2$  profiles inferred from MPS model runs, (D)  $\sigma_I^2$  inferred from COMSIC RO observations (Averages over Central pacific, New Mexico, and Arctic (North of Alaska), and (E)  $C_n^2$  derived from  $\sigma_I^2$  MPS model.